Synergistic Cooperation of Dual-Phase Redox Catalysts in Chemical Looping Oxidative Coupling of Methane

Leo Brody[1], Bar Mosevitzky Lis[2,3], Abigail Pérez Ortiz[4], Mohammadreza Kosari[1], Kyle Vogt-Lowell[1], Sam Portillo[1], Reinhard Schomäcker[4], Israel E. Wachs[2], and Fanxing Li[1*]

[1] Department of Chemical and Biomolecular Engineering, North Carolina State University, Raleigh, NC 27695-7905, USA

[2] Department of Chemical and Biomolecular Engineering, Lehigh University, Bethlehem, PA 18015, USA

[3] Department of Chemical Sciences and Bernal Institute, University of Limerick, Limerick, V94 T9PX, Ireland

[4] Institute for Technical Chemistry, Technische Universität Berlin, Berlin 10623, Germany

[*] *Correspondence author: fli5@ncsu.edu*

Abstract

Chemical looping oxidative coupling of methane (CL-OCM) presents a promising route for light olefin production, offering a simpler alternative to conventional methane steam reforming approaches. The selection of the redox catalyst used in CL-OCM is critical since it must achieve high C_{2+} yields (>25%) while maintaining longevity in harsh reaction environments. We present a comprehensive performance evaluation and characterization of an understudied, yet highly effective redox catalyst capable of achieving and maintaining a C_{2+} yield of 26.8% at 840°C. Through extensive *ex situ* and *in situ* analyses, including X-ray diffraction (XRD), near-ambient pressure X-ray photoelectron spectroscopy (NAP-XPS), and Raman spectroscopy, we characterized the catalyst and identified two distinct bulk, crystalline phases: cubic $Li_xMg_{6-x}MnO_8$ and orthorhombic $Mg_{3-x}Mn_x(BO_3)O_2$. Calcination at 1,200°C, as opposed to a typical calcination temperature of 900°C, increased the orthoborate oxide phase to ~45 wt.% while reducing the BET surface area by 65%. By investigating performance differences between these catalysts in their "sintered" and "pre-sintered" states, we have unveiled surprising cooperative effects between the two phases. Experiments with physical mixing of these two phases (granular stacking and mortar mixing) revealed that observed differences in CL-OCM efficacy cannot be solely due to sintering-induced loss of surface area but are also the result of synergistic, dual-phase interactions that enhance overall C_{2+} yield. H_2-temperarature programmed reduction (H_2-TPR) measurements and *ex situ* XPS analysis demonstrate that the sintered catalyst has a lower average Mn oxidation state which releases lattice oxygen more selectively and limits overoxidation to CO_x species. Additionally, NAP-XPS and *in situ* Raman characterization suggest that boron-oxygen coordinated sites (BO_x) may also play a role in improving selectivity. Leveraging insights from our phase mixture CL-OCM performance tests, steady-state experiments with co-fed O_2, and corroborative *in situ* characterizations, we propose that the synergistic interplay between $Li_xMg_{6-x}MnO_8$ and $Mg_{3-x}Mn_x(BO_3)O_2$ may be the result of facile oxygen release from the more redox-active $Li_xMg_{6-x}MnO_8$ phase combined with Li^+ migration to the orthoborate oxide phase.

Keywords: Chemical looping, Oxidative coupling of methane, Cooperative effects, Redox reactions, Boron.

1. Introduction

Methane (CH_4), the principal component of natural gas, is abundantly available yet presents significant challenges when used as a chemical feedstock. Its relatively low reactivity[1, 2], combined with the design complexities associated with conventional steam reforming approaches[3], motivates alternative conversion technologies. Oxidative coupling of methane (OCM) is a promising pathway for the direct catalytic conversion of methane to higher hydrocarbons, primarily ethylene and ethane (C_2H_4 and C_2H_6)[4]. This single-step process offers several advantages over steam reforming and pyrolysis strategies, such as being a simpler and thermodynamically favorable process with similar feedstock flexibility as reforming - accommodating both natural gas[5] and biogas[6, 7]. At present, the commercial implementation of OCM at scale is impeded by the limited yield of C_{2+} products, which results from unselective gas-phase and surface reactions, especially when operated under high methane conversion conditions[8]. These challenges have motivated researchers to consider alternative OCM reaction schemes and novel catalytic materials.

Since the overall OCM reaction is exothermic and exergonic, maximizing C_{2+} yield is hindered mainly by kinetics, the understanding of which remains an active area of research. While the reaction network of OCM is somewhat entangled, involving both heterogenous and homogenous reactions[9], the more fundamental steps of the pathway are generally agreed upon. Firstly, a catalyst aids in activating one of methane's C-H bonds to form gaseous methyl radicals ($CH_3\cdot$) that can then couple to form ethane[10]. Ethylene production proceeds in the gas phase through radical reactions as well as on the catalyst surface via catalytic ethane oxidative dehydrogenation (ODH). The undesired production of CO_x ($CO + CO_2$) species mainly transpires through the partial or complete oxidation of CH_4 and C_{2+} species in the gas phase. Although plug-flow reactors reduce the mixing of OCM products with molecular O_2, the necessity of co-feeding methane with gaseous O_2 presents challenges in preventing such nonselective reactions.

In contrast to the conventional co-feed mode, the chemical looping oxidative coupling of methane (CL-OCM) approach utilizes active oxygen species released from a reducible catalytic oxygen carrier or redox catalyst[11]. By this means, the OCM reaction is split into two subreactions: (i) a "reduction" step where the redox catalyst (M_xO_y) releases its lattice oxygen in a reducing atmosphere of CH_4 (Eq.1) and (ii) a subsequent "regeneration" reaction where the oxygen released are replenished by flowing a gas containing molecular O_2 (Eq.2). The CL-OCM scheme removes the need for a pure O_2 co-feed (and, therefore, a costly air separation unit) and eliminates direct contact between gaseous CH_4 and gaseous O_2, which reduces hot spot generation, improves process safety, and prevents further gas phase oxidation reactions [11-13]. The efficacy of CL-OCM, however, hinges upon the selection and design of suitable redox catalysts.

$$CH_4 + M_xO_y \rightarrow C_2H_6/C_2H_4 + H_2O + M_xO_{y-\delta} \quad (1)$$

$$M_xO_{y-\delta} + \frac{\delta}{2}O_2 \rightarrow M_xO_y \quad (2)$$

CL-OCM redox catalysts developed to date tend to incorporate manganese (Mn) as the reducible metal component, but catalytic materials reported in the literature also feature post-transition

metals as well as rare-earth elements including lanthanum[9, 14], cerium[15], and praseodymium[16]. Mn-based catalysts remain the most studied due to their high OCM activity, especially sodium tungstate-promoted manganese oxide supported on silica ($Mn\text{-}Na_2WO_4/SiO_2$) that has repeatedly demonstrated C_2 selectivities between 70-80% and CH_4 conversions between 20-30%[17]. First reported by Fang *et al*. in 1992[18], this catalyst has been studied in great detail by many researchers since then, primarily in the context of conventional OCM, yet the exact surface configuration and mechanistic role of the MnO_x and tungstate (WO_4^{2-}) sites remain a subject of debate[19-21]. For example, the role of the tungstate was previously regarded to be simply a stabilizer for preventing sintering and deactivation but has since been re-examined as a potential methyl-generation site in light of results uncovered by Wu and Li[17, 22] and expanded upon by Wang *et al*[23].

Alkali metal-doped Mg-Mn composite materials, although less explored, also show significant potential[24]. Specifically, Li-doped Mg_6MnO_8 has been demonstrated to be a promising redox catalyst for CL-ODH of ethane to ethylene[25] as well as for CL-OCM[26, 27]. Cheng *et al*. showed that Li-doping of Mg_6MnO_8 improved C_2 selectivity by 50%[27], while an extension study by Baser *et al*. found that co-doping with tungsten improved OCM performance by 330% (a C_{2+} yield of 28.6% was reported) compared to the undoped form[26]. Regardless of the metal constituents, effective redox catalysts should be recyclable, possess high oxygen-carrying capacities, and, more critically, release their lattice oxygen in a manner as to increase selectivity toward C_{2+} species[11].

Amidst the OCM research surge of the late 1980s, the Atlantic Richfield Company (ARCO) patented an array of boron-promoted (B-promoted) reducible Mn oxides containing alkali and alkaline earth metal components. In the 1988 ARCO patents by Sofranko *et al*.[28, 29], the inventors presented no less than five classes of catalyst compositions suitable for CL-OCM. The present work investigates one class of boron-promoted redox catalysts. Comparatively few researchers have explored these boron-containing CL-OCM catalysts. Notably, Chung *et al*. were the first to demonstrate these Mn-Mg-based catalysts for extended CL-OCM operation where they showcased the material's stability in a fixed-bed reactor for 100 cycles (>50 h), but their work did not include detailed catalyst characterization[13]. To our knowledge, an in-depth characterization of the material's bulk and surface properties has not been reported in the literature. More recently, attention has been drawn to the anti-overoxidation capabilities of boron-containing catalysts in ODH of propane to propylene[30-37] and ethane to ethylene[38-40], particularly for boron nitride and B_2O_3-based catalysts. Nevertheless, the exploration of B-promoted OCM catalysts remains under-investigated and narrowly focused on non-metallic materials[41, 42].

In this study, we systematically investigated the catalytic behavior of a highly effective Li-and B-promoted redox catalyst through CL-OCM performance testing and multiple *ex situ* and *in situ* characterization techniques. We examined two variants of this catalyst: one sintered at a high temperature of 1200°C and another at 900°C. We show that the reduction in surface area by sintering is insufficient to explain the selectivity enhancement of the sintered catalyst, but that in fact, compositional changes to the bulk structure reduce the number of less selective sites. Bulk phase identification reveals the presence of two major phases, cubic $Li_xMg_{6-x}MnO_8$ and orthorhombic $Mg_{3-x}Mn_x(BO_3)O_2$, which interact synergistically to improve C_{2+} selectivity. *In situ* characterizations (XRD, NAP-XPS, and Raman spectroscopy) aim to elucidate the time-resolved

bulk and surface compositional evolution of the catalytic species in CL-OCM reaction conditions. Additionally, CL-OCM evaluation of the two individual phases mixed in different configurations (granular stacking and mortar mixing) were conducted to investigate performance dependency on both composition and site-proximity while clarifying the role of each phase.

2. Materials and Methods

2.1. Catalyst Synthesis

The synthesis procedure generally followed the instructions laid out in "Example 5" of a 1988 ARCO patent [28]. In summary, powders of manganese dioxide (32.2 g), boric acid (11.3 g), magnesia (42.3 g, Materion), and lithium hydroxide (9.2 g) were ball milled with water and oven-dried at 80°C. Instead of performing one 16 h calcination at 900°C as laid out in the patent, the calcination process was divided into two parts: a 3-hour segment at 450°C followed by an 8-hour segment at 900°C. An additional "hardening" step was performed on one portion of the material that consisted of a 12 h calcination at 1,200°C. Henceforth, a distinction is drawn between the "pre-sintered" and "sintered" catalysts (calcined at 900 and 1200°C, respectively) in this article. For a comparative experiment, pure phases of $Li_{0.3}Mg_{5.7}MnO_8$ and $Mg_2Mn(BO_3)O_2$ were similarly synthesized via ball milling in water followed by calcination. Specifically, $Li_{0.3}Mg_{5.7}MnO_8$ was prepared by ball milling ~2.1 wt.% LiOH and Mg_6MnO_8, whose synthesis procedure is described in detail in our previous study[25], followed by an 8 h calcination at 950°C in still air. The $Mg_2Mn(BO_3)O_2$ phase was synthesized by ball milling stoichiometric amounts of Mn_3O_4, MgO, and B_2O_3 in water followed by a 12 h calcination at 1200°C in a tube furnace under airflow. Finally, all resulting powders were ground and sieved to the desired particle range for U-tube experiments of 300-450 μm.

2.2. Catalyst Testing

Steady-State Experiments

The steady-state OCM experiments were performed between 700 and 900°C and at ambient pressure. Approximately 50 mg of catalyst particles between 300-450 μm in diameter were placed into a 4 mm I.D. quartz tube and held in place on both sides by quartz wool. The tubular reactor was enclosed in an electric split tube furnace and inlet gases were controlled by Bronkhorst mass flow controllers. Temperature control was enabled via a thermocouple placed at the center, but outside of, the reactor tube. The furnace setpoint temperature and inlet gas flow rates were both monitored and regulated by a LabVIEW program. The reactor effluent was passed through a glass spiral reflux condenser for cooling and water removal prior to analysis by an online Agilent 7890A gas chromatograph.

CL-OCM Experiments

The CL-OCM experiments were performed in a quartz U-tube fixed-bed reactor with an 8 mm I.D. and 280 mm length. The quartz U-tube was centered in a Carbolite tube furnace for temperature control. The reactor was packed with 0.65 g of sintered material or 0.41 g of pre-sintered material to maintain the same gas hourly space velocity (GHSV) due to the difference in bulk densities of

the two materials, with 16-mesh alumina grit (Kramer Industries) on both sides of the catalyst bed performing as inert packing material to prevent blowout as well as preheat the inlet gas. An automated gas panel outfitted with Alicat mass flow controllers and Redhat solenoid valves, controlled by a LabVIEW program, was used to cyclically inject reducing (80% CH_4/Ar), purging (Ar), and oxidizing (80% O_2/Ar) gas mixtures into the reactor tube at timed intervals with the total feed flow rate held constant throughout the cycle. Most of the CL-OCM experiments were performed at 840°C and GHSVs of 1200 and 2400 h^{-1} to enable a direct comparison with the ARCO patent's results. In all CL-OCM experiments, the durations of the Ar purge and oxidation steps were 5 and 30 min, respectively.

The gaseous product stream exiting the reactor was fed to an MKS Cirrus II quadrupole mass spectrometer for real-time stream composition analysis. After the catalyst had been cycled three times under reaction conditions, gas samples were taken and were analyzed using an Agilent 7890 Series Fast RGA gas chromatograph with two thermal conductivity detector (TCD) channels (He/TCD channel for CO/CO_2 analysis and Ar/TCD channel for H_2 analysis) and a flame ionization detector channel for hydrocarbon analysis. Each gas sample consisted of filling a bag throughout the entire 15 or 30 s methane injection as well as a portion of the Ar purge step to ensure that the gaseous products from the OCM step are fully collected (Fig. S1). From the obtained GC measurements of the outlet gas carbon percentages (C_i), the time-averaged gas-phase conversion of methane (χ_{CH_4}), C_{2+} selectivity ($S_{C_{2+}}$), and C_{2+} yield ($Y_{C_{2+}}$) are calculated on a carbon basis using the following equations:

$$\chi_{CH_4} = 1 - C_{CH_4} \tag{3}$$

$$S_{C_{2+}} = \frac{\sum \mu_i C_{2+,i}}{1 - C_{CH_4}} = \frac{Y_{C_{2+}}}{\chi_{CH_4}} \tag{4}$$

where μ_i is the number of C atoms in each $C_{2+,i}$ product. The specific productivity of the catalyst, defined as the moles of C_{2+} species produced normalized by the catalyst surface area and injection time, was calculated using the measured $Y_{C_{2+}}$ from the GC data multiplied by the total moles of methane injected (which gives moles of C_{2+} species); (ii) the BET-obtained surface area ($m^2 \cdot g^{-1}$) multiplied by the mass loading of the catalyst to obtain the surface area of the catalyst in m^2; and (iii) the injection time of the methane.

2.3. Catalyst Characterizations

XRD and Rietveld refinement

Ex situ bulk phase identifications of pre-sintered and sintered samples were conducted using a Rigaku SmartLab X-ray diffractometer (Bragg-Brentano geometry) with Cu Kα (λ = 0.1542 nm) radiation operating at 40 kV and 44 mA. A scanning range of 10-65° (2θ) with a step size of 0.05° holding for 3.0 s at each step was used to generate XRD patterns. After the identification of candidate phases in HighScore, all obtained XRD patterns were refined using the Rietveld program General Structure Analysis System II (GSAS-II) [43] to quantify lattice parameters, phase percentages, site occupancy fractions, and mean crystallite sizes. Refined parameters included the scale factor, specimen displacement, background (modeled Chebyshev-1 model with 6

parameters), phase fraction, crystallite size, microstrain, lattice parameters, atomic positions, and occupancy fractions.

In situ XRD was performed with an Empyrean PANalytical diffractometer using Cu Kα radiation operating at 45 kW and 40 mA. A scanning range of 10-65˚ (2θ) with a step size of 0.03˚ holding for 0.4 s at each step was used to generate XRD patterns. Temperature-programmed experiments were performed whereby the samples were ramped under air at a rate of 10°C·min^{-1} to 840°C and, after a 15 min purge under Ar, 4% CH_4/Ar was introduced for 90-135 minutes depending on the reducibility of the sample. An additional 15 min Ar purge would follow, and finally regeneration under air for 30-45 min.

XPS, HRTEM-EDX and SEM-EDS

Analysis of the surface region (1-3 nm) was carried out on a Kratos Analytical Axis Ultra X-ray photoelectron spectroscopy (XPS) spectrometer using a monochromatic Al Kα X-ray source. Emission amperage and tension were set at 10 mA and 15 kV respectively. In addition, charge neutralization was enabled during sample acquisition. For each sample, a single survey scan was performed in the range of 0-1200 eV with a pass energy of 160 eV, step energy of 1 eV, and dwell time of 200 ms. For high-resolution region scans, 5 scans were performed for each element of interest with a pass energy of 20 eV, step energy of 0.1 eV, and dwell time of 500 ms. The resulting spectra were analyzed using CasaXPS, with corrections for surface charging made by adjusting the adventitious C 1s peak to 284.8 eV.

Surface morphology and bulk elemental distribution were assessed via field emission scanning electron microscopy (SEM) and energy dispersive spectroscopy (EDS), respectively, using a Hitachi SU3900 SEM with Oxford Ultim Max 40 EDS in variable pressure mode. A pressure of 70 Pa was used, and the SEM images were taken in backscatter mode at 20 kV. Additionally, high-resolution transmission electron microscopy (HRTEM) and scanning transmission electron microscopy with high-angle annular dark-field imaging (STEM-HAADF) coupled with energy dispersive X-ray (EDX) were utilized to further characterize the morphology and bulk elemental composition (by STEM-EDX mode) of the catalytic samples (Fischer Scientific Talos, operating at 200 kV).

H_2-TPR

Temperature-programmed reduction with hydrogen (H_2-TPR) was conducted in a Micrometrics® AutoChem II instrument equipped with a TCD detector. For each experiment, ~0.1 g of material was used, and a preliminary dehydration step was conducted whereby the sample was ramped up at a rate of 10°C·min^{-1} under pure He (50 SCCM) to 400°C for 1h, then cooled down to 100°C and held at that temperature for 20 min before the onset of the H_2-TPR ramp. The sample was then ramped at 10°C·min^{-1} under 10% H_2/Ar to 950°C and held at temperature for 20 min before the final cool down.

BET Surface Area

The Brunauer−Emmett−Teller (BET) surface area of both sintered and pre-sintered samples using N_2 was measured at 77 K with a physisorption apparatus (Micrometrics ASAP 2020) via a multipoint physical measurement.

ICP-OES

Inductively coupled plasma-optical emission spectroscopy (ICP-OES) was used for elemental and compositional analysis using a 715-ES-inductively coupled plasma analysis system with a CCD detector (Varian). For sample preparation, 50 mg of catalyst powders were dissolved in a mixture of 3 vol% nitric acid in water.

In situ Raman Spectroscopy

For the *in situ* Raman experiments, a Horiba LabRAM HR Evolution confocal Raman microscope equipped with a 442 nm excitation wavelength laser source (Kimmon IK-Series He-Cd Laser, filtered to ~18 mW at the objective) and a thermoelectrically cooled Horiba Synapse BIDD scientific CCD camera detector were used to acquire the *in situ* Raman spectra maps. The laser was focused onto the samples with a 10x objective (Olympus BX-30-LWD) while the spectrometer was used with a 500 nm grating and a 100 μm hole, resulting in a spectral resolution of ~2.5 cm^{-1}. The 520.7 cm^{-1} band of a silicon wafer standard was used to calibrate the spectrometer before spectral acquisition. Powder catalysts were loaded into a quartz wool-padded reaction cell (Linkam Scientific Instruments CCR-1000) and connected to a gas flow control system. A Linkam Scientific Instruments T96-HT unit controlled the catalyst temperature and a heating/cooling rate of 10°C·min^{-1} was used throughout the *in situ* experiments. Samples were mapped over 36 spots on a 500 μm x 500 μm grid, moving to a different region on each sample before acquiring sequential maps. Samples were first heated to 840°C under 10% O_2/Ar flow, and after 30 minutes under those conditions, mapped. This was followed by purging with Ar, switching to 1.5% CH_4/Ar and holding under those conditions for 30 minutes, at which point the samples were again mapped. Finally, after purging with Ar, switching back to 10% O_2/Ar and holding under those conditions for an additional 30 minutes, a final map was acquired.

NAP-XPS

For the Near Ambient Pressure X-ray Photoelectron Spectroscopy (NAP-XPS) experiments, a SPECS DeviSim NAP reactor coupled with a PHOIBOS 150 NAP electron energy analyzer was used to acquire the *in situ* XPS spectra. Hardened catalyst powder was pressed onto an SS 316 mesh and then secured onto a stainless-steel sample holder with a type K thermocouple which was heated using an e-beam heater. The Mn 2p, O 1s, Mg Auger, C 1s, B 1s, and Li 1s spectra were acquired with a 0.05 eV resolution and a pass energy of 70 eV at a pressure of ~1.5 mbar. The sample was heated to 600°C under a flow of 80% O_2/Ar, switching sequentially to flows of Ar, 80% CH_4/Ar, and 80% O_2/Ar again while holding for 1 hour at the same temperature before acquiring spectra under each atmosphere. The measurement spot was changed each time to circumvent possible accumulative beam-damage influence prior to subsequent spectra acquisitions. The resulting spectra were analyzed using CasaXPS, with corrections for surface charging made by adjusting the adventitious C 1s peak to 284.8 eV.

3. Results and Discussion

3.1. CL-OCM Performance and Redox Behavior

From the same precursors, we synthesized and examined two catalyst systems differentiated by their calcination procedures: one catalyst is ball milled and calcined at 900°C (denoted as pre-sintered), while the other undergoes an additional calcination or "sintering" step afterward at 1200°C (denoted as sintered). The difference in CL-OCM performance between the sintered and pre-sintered catalysts at two distinct GHSVs (1200 and 2400 h^{-1}) and injection times (15 and 30 s) at a constant reactor temperature (840°C) is illustrated in Fig. 1(a). While both catalysts exhibited higher C_{2+} selectivity (ranging from 64.5% to 84.1%) at the higher GHSV, the conversion showed a stronger dependence on injection time. Decreasing the injection time by half increased the conversion, but this relationship was less pronounced at the higher space velocity conditions. This indicates that methane activation occurs towards the beginning of the injection and diminishes as active oxygen species are consumed. The peak conversion for both samples was witnessed at 1200 h^{-1} with a 15 s injection time, but even in this case, the sintered catalyst's conversion (35.4%) remained lower than the lowest observed value for the pre-sintered sample (36.4%). The pre-sintered catalyst achieved the highest C_{2+} yield of 26.8% at 840°C. This strong performance motivated additional cycling at the same condition to assess longevity. After 30 CL-OCM cycles in the U-tube reactor, the measured yield deviated by ~0.4% (final conversion of 41.1% and selectivity of 65.4% giving a yield of 26.9% vs. initial value of 26.8%) from the initial value, demonstrating significant promise for sustained packed-bed reactor operations. ICP-OES measurements validated that most of the Li remained in the spent catalyst even after cycling (Fig. S2(a&b)). It is also noted that minor Li-containing phases ($LiMnO_2$ and Li_2MnO_4) emerged from the redox cycles, in addition to the $Li_xMg_{6-x}MnO_8$ phase in the as-prepared sample (Fig. S3).

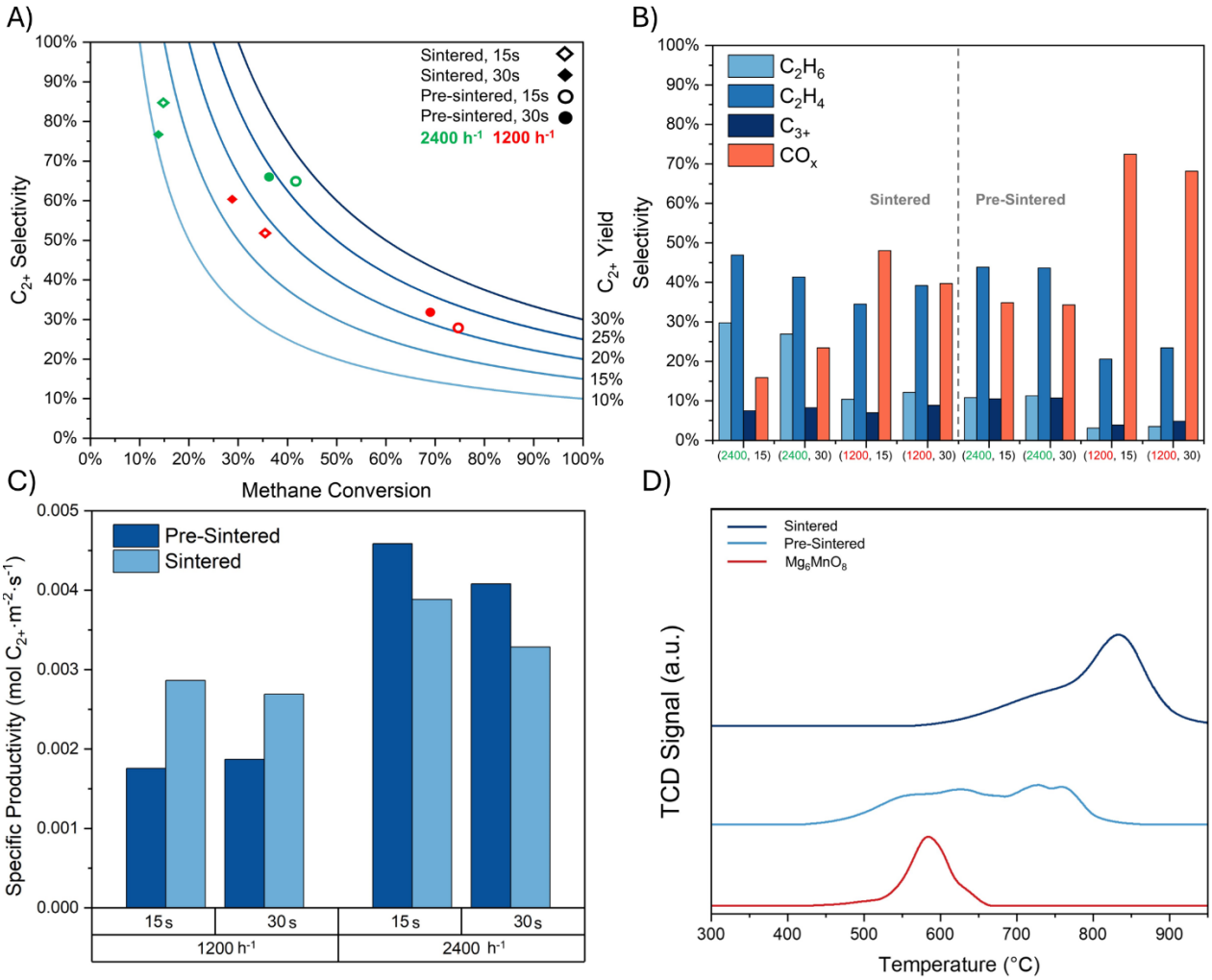

Figure 1. (a&b) Performance data (C_{2+} yields and selectivities) summaries comparing the pre-sintered and sintered samples at fixed temperature of 840°C and variable GHSV and injection time; **(c)** specific productivity of each catalyst defined as the moles of C_{2+} produced normalized by surface area and injection time; and **(d)** H_2-TPR profiles of the sintered, pre-sintered, and undoped Mg_6MnO_8 catalysts.

The pre-sintered catalyst is more active to CO_x formation when compared to the sintered catalyst at the same reaction conditions (Fig. 1(b)). Notably, at lower GHSV and injection time, the pre-sintered catalyst had a 72% CO_x selectivity, about 50% higher than the sintered catalyst's 48%. When comparing the ratio of C_2H_4/C_2H_6 selectivities at each condition, the value for the pre-sintered catalyst is always higher. However, at the higher GHSV condition, the ethylene selectivities between the two catalysts are similar. This trend highlights the challenge of OCM where higher methane conversion always leads to increased CO_x selectivity. For example, at the higher GHSV, the pre-sintered material's C_2H_4 selectivity remains greater than its CO_x selectivity, highlighting the importance of sufficiently short residence times to avoid oxidation of the OCM products. The C_{2+} yield of the sintered catalyst can be driven above 20% by increasing the temperature to 875°C (Fig. S4). Conversely, the pre-sintered catalyst boasts a ~23% yield even at 825°C but loses virtually all C_{2+} selectivity at 875°C and 1200 h^{-1} GHSV. As for the C_{3+} selectivity, the maximum (10.8%) was witnessed at the higher injection time and GHSV condition (Table S1).

A breakdown of CO_x selectivity into individual CO and CO_2 proportions at each condition is presented in Table S2. For both catalysts, CO_2 is the predominant species, making up 69-82% of the CO_x selectivity, with the highest CO_2 selectivities witnessed at the lower GHSV condition. In general, CL-OCM is known to produce a higher range of hydrocarbon products compared to co-feed OCM, spanning C_2-C_7 species[11]. The lowest C_{3+} selectivity occurs with the more active pre-sintered catalyst at the lower GHSV condition, where, akin to an O_2 co-feed environment, any produced C_{4+} hydrocarbons are oxidized in the gas phase to CO_x. The formation of C_{6+} species was not witnessed under any conditions. Additionally, online monitoring of the gaseous products via mass spectrometry showed no CO_2 formation during the regeneration steps, indicating that coke formation was minimal.

BET analysis of N_2 isotherms, unsurprisingly, indicated that high-temperature sintering of the catalyst decreased the catalyst's surface area by 65% from 1.03 to 0.36 $m^2 \cdot g^{-1}$, with a concurrent 50% increase in the bulk density from 0.68 to 1.05 $g \cdot mL^{-1}$. By normalizing the production of C_{2+} species by surface area and injection time at each condition (defined as specific productivity as shown in Fig. 1(c)), we can more accurately discern the role of surface area. The surface area normalized specific productivity differences between the two catalysts fall within a 15-30% range, on a relative basis, for the high GHSV cases. Under low GHSV conditions, the relative difference increased to 43 – 63%. This magnitude of difference suggests that performance is impacted by factors in addition to surface area. The H_2-TPR measurements reinforce this assumption (Fig. 1(d) and Fig. S5) which clearly illustrate a shift of reduction temperature. The reference catalyst, undoped Mg_6MnO_8, readily releases lattice oxygen in a reducing atmosphere even at T<600°C, while at the other extreme, the sintered catalyst is reduced only when the temperature exceeds 800°C.

In CL-OCM applications the oxygen-release from the redox catalyst is typically inversely related to the C_{2+} selectivity, therefore we may expect that the more active redox catalysts have higher weighted oxygen release values (mg O/mg catalyst) with correspondingly lower C_{2+} selectivities. The trends in oxygen release for both the pre-sintered and sintered variants, as depicted in Fig. S6, align with the performance outcomes summarized in Fig. 1(a&b). Specifically, the pre-sintered variant demonstrates a higher oxygen release per mass of catalyst under all conditions, with longer injection times and lower GHSVs resulting in greater oxygen release. Additionally, the sensitivity of C_{2+} selectivity to GHSV and injection time is apparent as well, with the higher GHSV yielding the higher selectivity.

3.2. Catalyst Bulk Structure, Morphology, and Surface Composition/Oxidation States

To explain the apparent differences in CL-OCM performance, we sought to rigorously characterize the redox behavior of the two catalysts. *Ex situ* powder XRD characterization revealed a noticeable compositional difference between the pre-sintered and sintered catalysts (Fig. 2(a)). Rietveld refinement of the resulting diffraction patterns was used to quantify the different phases in the sample by their corresponding mass fractions (Fig. S7). The refinement statistics along with the refined parameters can be found in Table S3. In both the pre-sintered and sintered samples, the dominant phases were Murdoch-type Li-doped Mg_6MnO_8 (denoted as $Li_xMn_{6-x}MnO_8$) followed by the Ludwigite class of Mg-Mn orthoborate oxide (denoted as $Mg_{3-x}Mn_x(BO_3)O_2$). 1200 °C

sintering of the catalyst resulted in a decrease in the wt% of $Li_xMn_{6-x}MnO_8$, from 72.5% to 54.3% with a concurrent increase in the wt% of $Mg_{3-x}Mn_x(BO_3)O_2$ from 19.3% to 45.7%. The remaining 8.2 wt% of the pre-sintered material is represented by minor phases that are converted during the high-temperature calcination as shown in Fig. 2(b&c). Additionally, the pattern refinement showed that sintering substantially increased the crystallite size, which is also substantiated by SEM micrographs (shown in Fig. 2(d&e)) and reflected in the significant decrease in surface area. In addition, HRTEM and its respective STEM-EDX elemental mappings of the catalysts (illustrated in Fig. S9 and quantified in Table S4) exhibit uniform elemental distribution, except for boron, without any localized elemental aggregation or segregation. The localization of boron in one fragment of the particles shown in Figure S9(c) may indicate that one fragment is richer in the orthoborate oxide phase than the other.

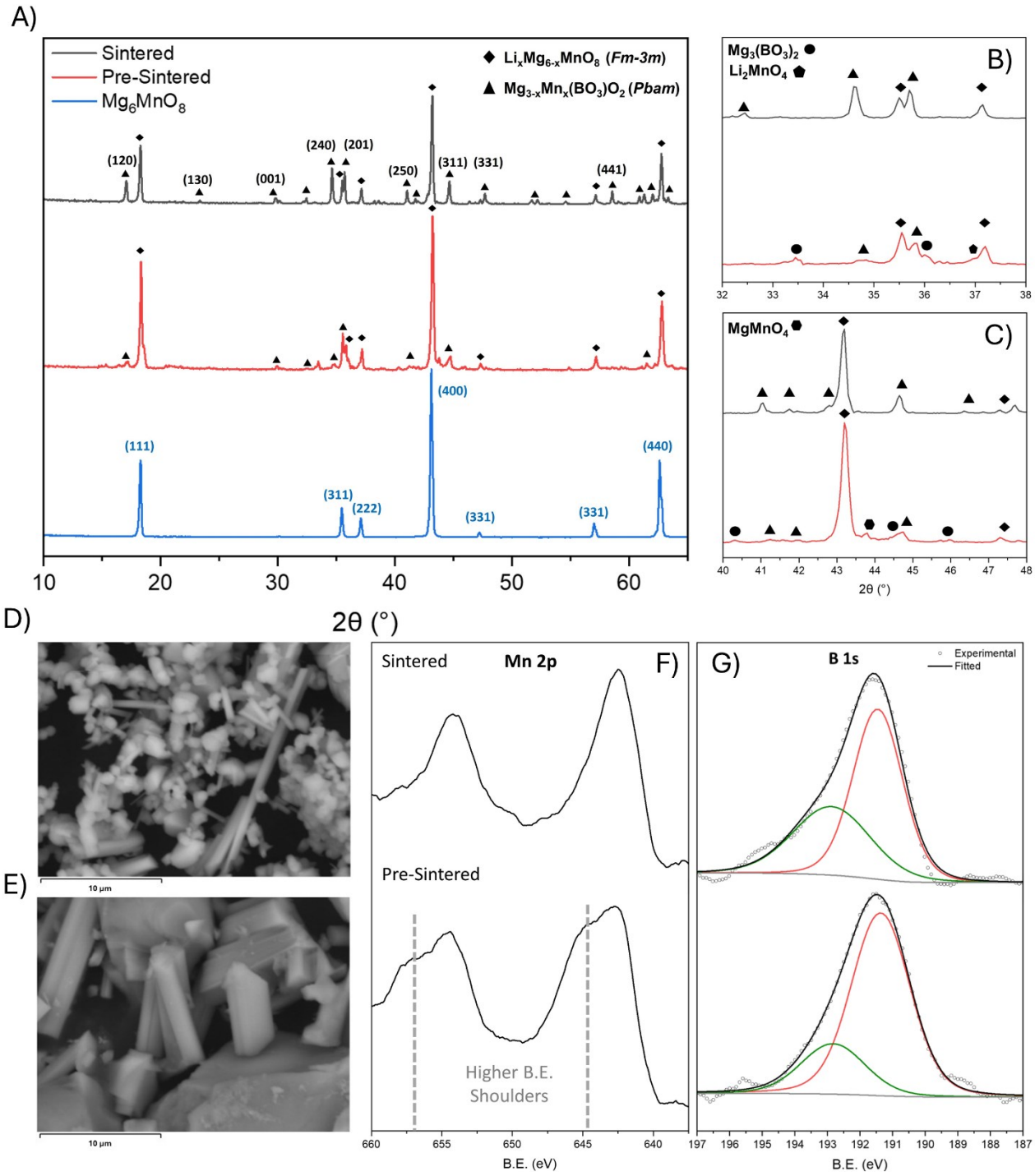

Figure 2. XRD patterns **(a)** comparing pre-sintered and sintered samples with magnified regions at **(b)** 32-38°2θ and **(c)** 40-48°2θ detailing the disappearance of minor phases and increasing intensity of the (240) and (201) families of planes from $Mg_{3-x}Mn_x(BO_3)O_2$. SEM micrographs (10 µm resolution) of the **(d)** pre-sintered and **(e)** sintered catalysts. XPS spectra of the **(f)** Mn 2p and **(g)** B 1s features for both catalysts.

The XPS spectra of the surface region (1-3 nm) plotted in Fig. 2(f and g) unveil notable differences in the cation oxidation states between the two catalysts despite similar surface atomic compositions (quantified on a C-free basis in Table S5). For Mn, the only reducible component, distinct features

can be parsed out from the XPS Mn 2p spectra that signify an apparent difference in average surface oxidation states (Fig. 2(f)). Since Mn has three oxidation states (II, III, and IV) that exhibit multiplet splitting with overlapping BE ranges, we have not attempted to deconvolute the Mn 2p spectra and choose instead to make a qualitative assessment of the average surface Mn oxidation state differences between the two samples. A large shoulder signifying a second peak at 644.7 eV can be seen in the pre-sintered catalyst. This peak is suggestive of $Mn^{4/5+}$ cations, drawing upon studies using MnO_2 standards[44, 45]. In the case of surface boron species, both the pre-sintered and sintered catalysts exhibit a conspicuous peak at binding energies (BE) between 191.36-191.45 eV in the B 1s spectra (Fig. 2(g)). Multiple studies utilizing XPS to characterize borate-containing compounds have assigned the B^{3+} core level in the orthoborate anion (BO_3^{3-}) to within the range of 191.4-191.8 eV in the B 1s spectra [46-49]. A second peak can be seen for both samples at 192.8 eV. This peak is likely attributable to B_2O_3, which is known to display peaks in the range of 192.4-194.5 eV[50]. While crystalline B_2O_3 was not identified in the XRD patterns for either catalyst, the near-surface sensitivity of XPS could detect B_2O_3 that is not resolved in the XRD patterns.

3.3. In Situ Characterization in Reducing and Oxidizing Environments

NAP-XPS measurements were conducted at 600°C on the sintered catalyst in a CL-OCM environment mirroring the same experimental gas compositions (i.e., 80% CH_4 in Ar for the OCM step) to evaluate possible changes in the surface chemical environment. While this *in situ* XPS experiment significantly narrowed the temperature and pressure gaps between experimental and *in situ* characterization conditions, the relatively low-temperature (600°C) and low-pressure (1.5 mbar) environment means that only subtle changes in oxidation state and chemical coordination of the cations in the surface region are visible (Fig. 3) when compared to the actual OCM conditions. Nonetheless, hints of surface CL-OCM activity are seen in the spectra. For the Mn 2p spectra (Fig. 3(a)), as was the case for the *ex situ* scans, a slight broadening of the Mn $2p_{3/2}$ peak occurs during the oxidation steps, and a narrowing during the reduction step, suggesting a slight decrease in the average Mn oxidation state in the surface region. What is more interesting, however, is the appearance of a higher BE shoulder in the B 1s spectra during the injection of methane (Fig. 3(b)). Deconvolution reveals two peaks: the main peak, comprising ~95% of the peak area, occurs at 191.45 eV and is assigned to BO_3^{3-} and the second peak is positioned at 193.45 eV, which is 0.65 eV higher than the previously observed *ex situ* BE values for B_2O_3, but well within the range of literature-reported values. The disappearance of the ~192.8 eV peak detected at room temperature further substantiates that the surface boron species is dynamic under OCM reaction conditions. This higher B.E. peak at 193.45 eV was also observed by Shi et al.[38] and Grant et al. [31] in the context of ethane and propane ODH and was attributed as an active species contributing to C-H bond activation.

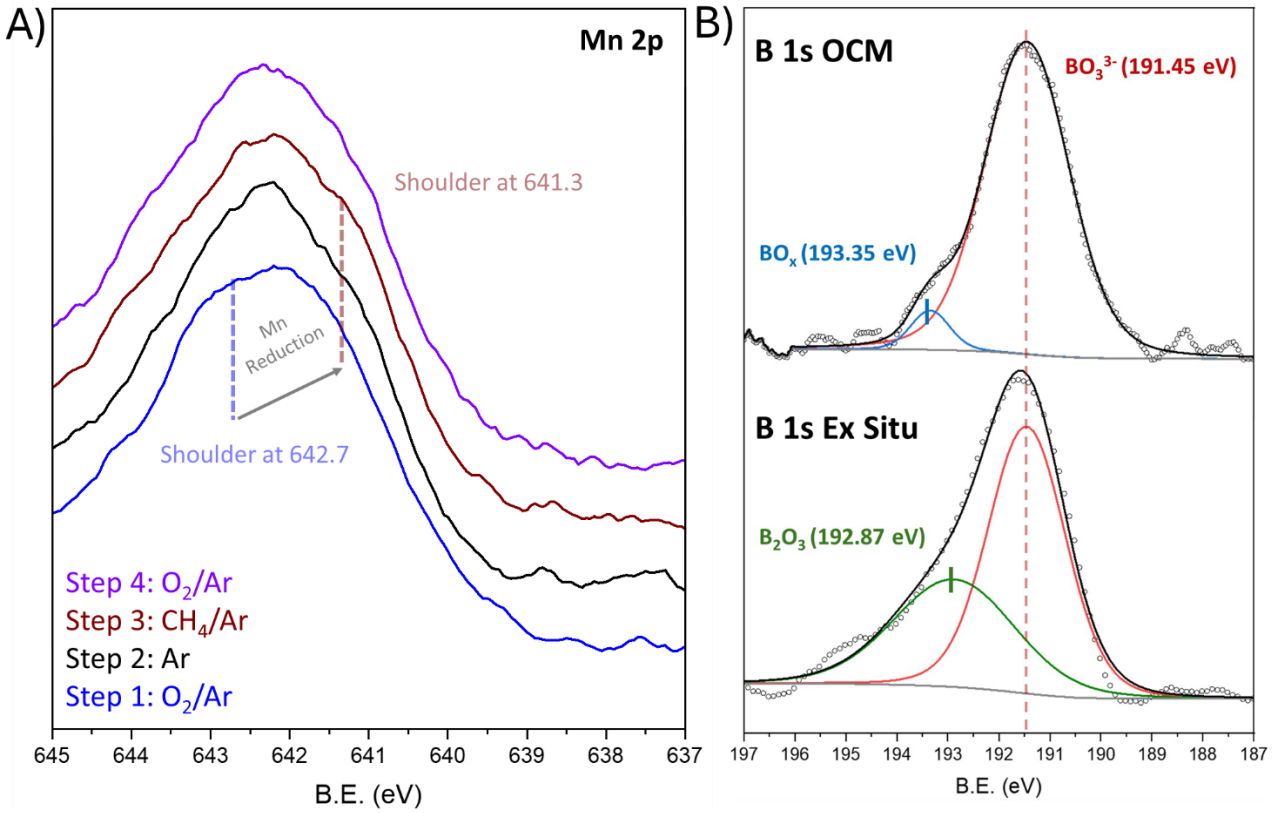

Figure 3. XPS spectra of the sintered catalyst: **(a)** Mn $2p_{3/2}$ (*in situ*), and **(b)** B 1s (*in situ*), with B 1s (*ex situ*) for comparison purpose.

In situ XRD was conducted at 840°C to evaluate the dynamic bulk phase evolution in an approximate CL-OCM environment (Fig. 4). No phase changes were witnessed during the ramp from room temperature to 840°C under air, which affirms that the phases identified in Fig. 2(a) from *ex situ* XRD are the same present at the start of the CL-OCM cycle. The same planes identified in Fig. 2(a) for both $Li_xMg_{6-x}MnO_8$ and $Mg_{3-x}Mn_x(BO_3)O_2$ can be seen at both the start and end of the CL-OCM cycle, signifying a rapid and complete regeneration to the starting phases and further demonstrating that these materials are favorable for repeated cycling. For both catalysts, prolonged exposure to a reducing environment (4% CH_4/Ar) results in the reduction of $Li_xMg_{6-x}MnO_8$ to (Mn,Mg)O. This change is apparent from the complete loss of the (111), (311), (222), and (511) planes for $Li_xMg_{6-x}MnO_8$ and the shift of the major (400) and (440) peaks to those of (200) and (220) for Li-doped (Mn,Mg)O as seen in Fig. 4(c&d). Meanwhile, the peaks ascribed to the $Mg_{3-x}Mn_x(BO_3)O_2$ phase diminish in intensity somewhat, perhaps due to some degree of lattice oxygen release, but do not completely disappear. This observation is consistent with the low oxygen release witnessed for $Mg_2Mn(BO_3)O_2$ in OCM experiments presented in subsequent sections. In particular, the most intense orthoborate oxide peaks corresponding to the (240) and (201) planes remain visible throughout the reduction step for both catalysts. From this time-resolved bulk phase analysis, there was no clear evidence of the formation of $(Mg,Mn)_2B_2O_5$, the most likely candidate for a reduced phase of $Mg_{3-x}Mn_x(BO_3)O_2$, which would present major peaks at 19° and 31.4°. Therefore, if the orthoborate oxide does not visibly change its phase to a reduced

form after >90 min of exposure to a reducing environment, then 15-30 s of exposure during the actual CL-OCM experiments is unlikely to fully reduce it either.

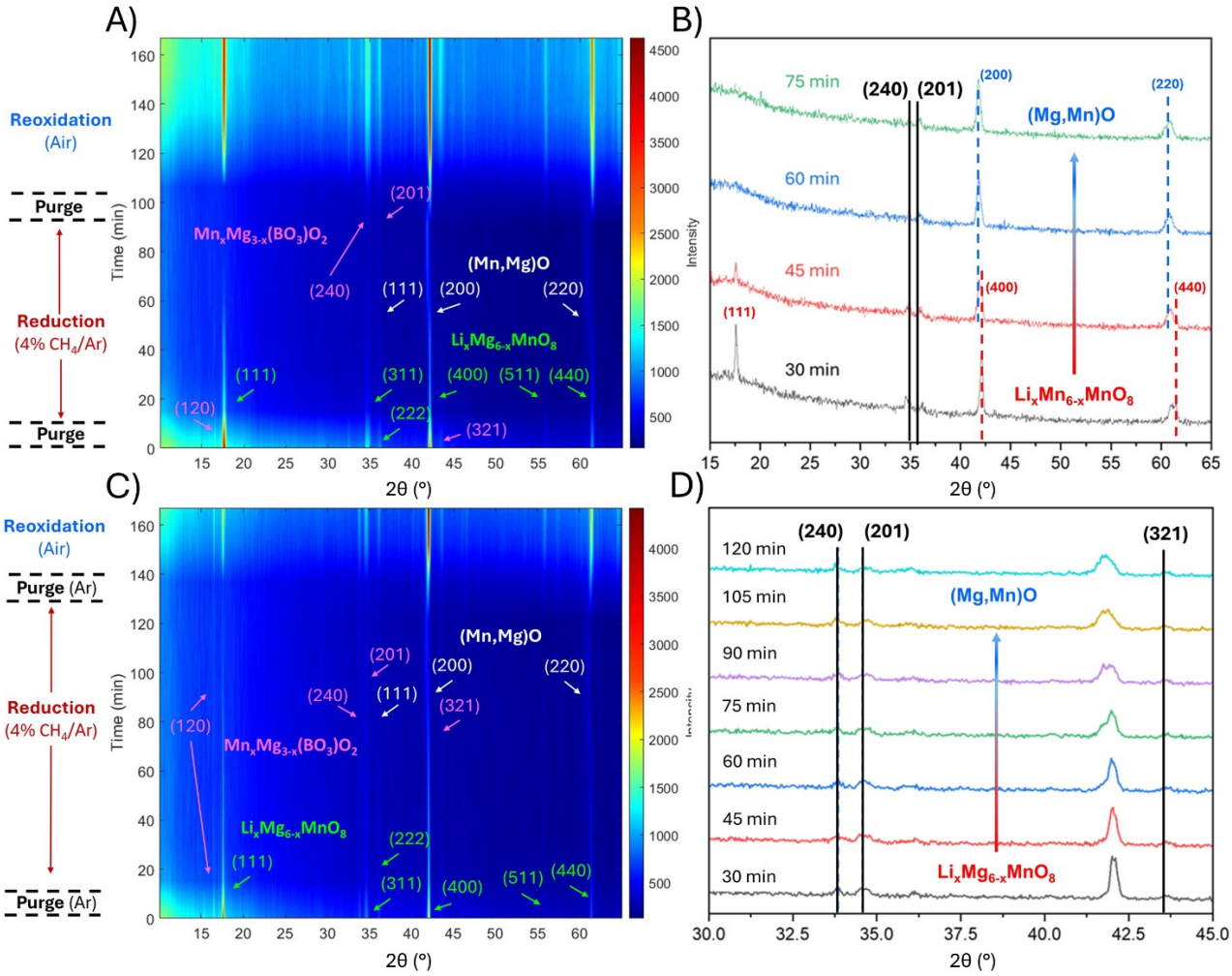

Figure 4. *In situ* XRD patterns of the as a function of time at 840°C for **(a&b)** pre-sintered and **(c&d)** sintered catalysts under reducing and oxidizing environments.

In situ Raman spectroscopy measurements were conducted to identify potential phases lacking long-range order that would not be readily apparent from the XRD patterns as well as to visualize the structural dynamics more clearly in isothermal oxidizing and OCM reaction environments at 840°C (Fig. 5(a&b)). To improve the precision of band assignment, Raman spectra were also collected for $Li_{0.3}Mg_{5.7}MnO_8$ and $Mg_2Mn(BO_3)O_2$ (Fig. 5(c&d)). For both the pre-sintered and sintered catalysts, a strong Raman band at ~587 cm^{-1} and a weaker band at ~451 cm^{-1} can be seen during the oxidation steps. These same bands appear very prominently for the pure $Li_{0.3}Mg_{5.7}MnO_8$ sample and likely arise from vibrations associated with asymmetric and symmetric stretching of the MnO_6 octahedra since LiO_x and MgO_x do not give rise to strong Raman bands due to the ionic character of their M-O bonds[51]. The location of the higher-frequency band at 587 cm^{-1} is supported by the findings of Julien *et al*. who showed that Li-doping of birnessite (δ-MnO_2) results in significant spectral modifications due to the nature and location of the ions between the MnO_6 octahedra sheets[52]. Moreover, these bands disappear during the OCM step, signifying the collapse

of the MnO_6 octahedra via lattice oxygen release upon Mn reduction, but reappear in the final oxidizing step. When no Li is present, as is the case with the $Mg_2Mn(BO_3)O_2$ phase, the position of this higher-frequency MnO_6 band shifts upward and can be detected at ~657 cm^{-1}, but is still within the range of expected MnO_6 vibrations from the literature[52, 53].

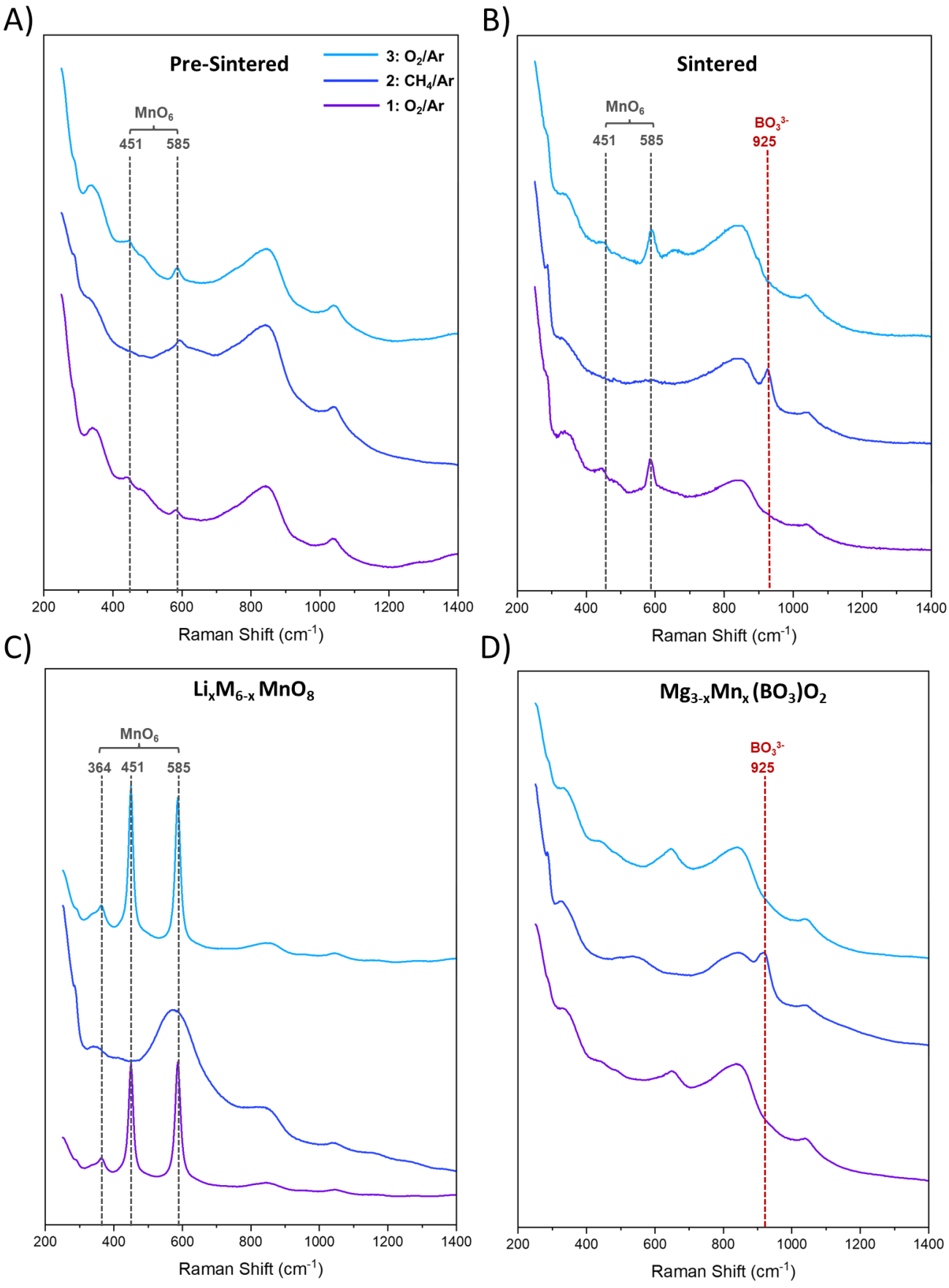
A)
Pre-Sintered
3: O2/Ar
2: CH4/Ar
1: O2/Ar
MnO6
451
585
Raman Shift (cm-1)
B)
Sintered
MnO6
451
585
BO3 3-
925
Raman Shift (cm-1)
C)
LixM6-x MnO8
MnO6
364
451
585
Raman Shift (cm-1)
D)
Mg3-xMnx(BO3)O2
BO3 3-
925
Raman Shift (cm-1)

Figure 5. *In situ* Raman spectra (normalized to the 840 cm^{-1} band) collected under two different gas environments (oxidizing and reducing) at 840°C of four different catalysts including (**a**) pre-sintered, (**b**) sintered, (**c**) $Li_{0.3}Mg_{5.7}MnO_8$, and (d) $Mg_2Mn(BO_3)O_2$.

The disappearance of bands ascribed to MnO_6 octahedra vibrational modes coincides with the emergence of a relatively sharp band at ~925 cm^{-1} in the Raman spectrum of the sintered and $Mg_2Mn(BO_3)O_2$ catalysts. Previous studies investigating orthoborate glasses[54, 55] assigned this band to symmetric stretching of B-O bonds of the orthoborate anion BO_3^{3-}, which belongs to the crystalline orthoborate oxide phase previously identified by XRD. The appearance of this band during the OCM reduction could suggest that the reduction of the MnO_6 octahedra in the orthoborate oxide phase may involve oxygen reconfiguration that either stretches the BO_3^{3-} anion or changes its geometry from 3-fold oxygen coordinated to 4-fold[56]. Reconfiguration of BO_3^{3-} from a trigonal planar to tetrahedral coordination is less likely given that the B-O stretching of BO_4 units should manifest a clear peak at ~1030 cm^{-1} as well as others at 900 and 940 cm^{-1}[57]. Since *in situ* XRD revealed no obvious structural transitions of $Mg_{3-x}Mn_x(BO_3)O_2$, but did indicate some degree of lattice oxygen release, then it is possible that oxygen vacancy formation from the Mn^{3+} to Mn^{2+} reduction occurred without significant change to the crystal structure but induced local configurational changes to the BO_3 groups that rendered them more Raman active.

3.4. Investigation of Phase Interactions and Synergy

To probe the role of individual phases within these complex redox materials, the two main crystalline phases ($Li_{0.3}Mg_{5.7}MnO_8$ and $Mg_2Mn(BO_3)O_2$) were synthesized and tested in identical CL-OCM conditions individually as well as in two different mixture configurations (granular stacking and mortar grinding) to assess the effect of site proximity (Fig. 6(a&b). The experiments outlined in this section were all performed at the same conditions: 30 s methane injection time, GHSV of 2400 h^{-1}, and temperature of 840°C. The CL-OCM performance of the two phases individually was poor, with neither exceeding a 5% C_{2+} yield. The $Li_{0.3}Mg_{5.7}MnO_8$ catalyst displayed significantly higher activity (33-40% methane conversion) than the orthoborate oxide phase (<10% methane conversion) but with lower C_{2+} selectivity (12-16%) than the orthoborate oxide phase (20 – 27%). In evaluating the role of site proximity, we tested two physical mixing scenarios: granular stacking and mortar grinding. For the granular mixture of both phases, the particle size was fixed between 300-425 μm to align with previous experiments, and the same nominal phase distribution as the sintered catalyst discerned by the Rietveld refinement was maintained (i.e., 54% $Li_xMg_{6-x}O_8$ and the balance $Mg_{3-x}Mn_x(BO_3)O_2$). The granular stacking configuration increased the yield to ~10% due to the higher selectivities and only slightly reduced conversions. Further reducing site distance by mortar-grinding of the phases and pelletizing/sieving the powder to particles in the 300-425 μm mesh range (without further sintering) resulted in a slight C_{2+} selectivity enhancement, though yields remained below 10%.

As a further measure to increase phase proximity, three mortar-ground compositions were prepared corresponding to 20/80, 50/50, and 80/20 mixtures by weight of the orthoborate oxide phase (B) and the $Li_{0.3}Mg_{5.7}MnO_8$ phase (L), respectively, and then calcined at 900°C (Fig. 6(a&b)). Adding 20 wt.% B to L resulted only in a "dilution effect" whereby the C_{2+} yield remains the same, but the conversion and selectivity move in opposing directions. However, when 20 wt.% L is mixed with B, an enhancement effect is witnessed where the yield increases. Finally, the 50/50 mixture

demonstrated a clear enhancement effect with C_{2+} selectivity approaching that of the original sintered catalyst. The yield trend suggests that the enhancement effect of mixing the two phases has a volcano-type dependence on composition. As a point of comparison, the XRD patterns of the original sintered catalyst and the 50/50 mixture are presented in Fig. 6(c), largely showing close resemblance. Besides reducing the distance between the two phases, sintering of the mortar-ground mixture at 900°C is likely to promote the exchange of cations between the two phases such as lithium (from L to B) and boron (from B to L), leading to increased selectivity by promoting the active sites, as will be discussed next.

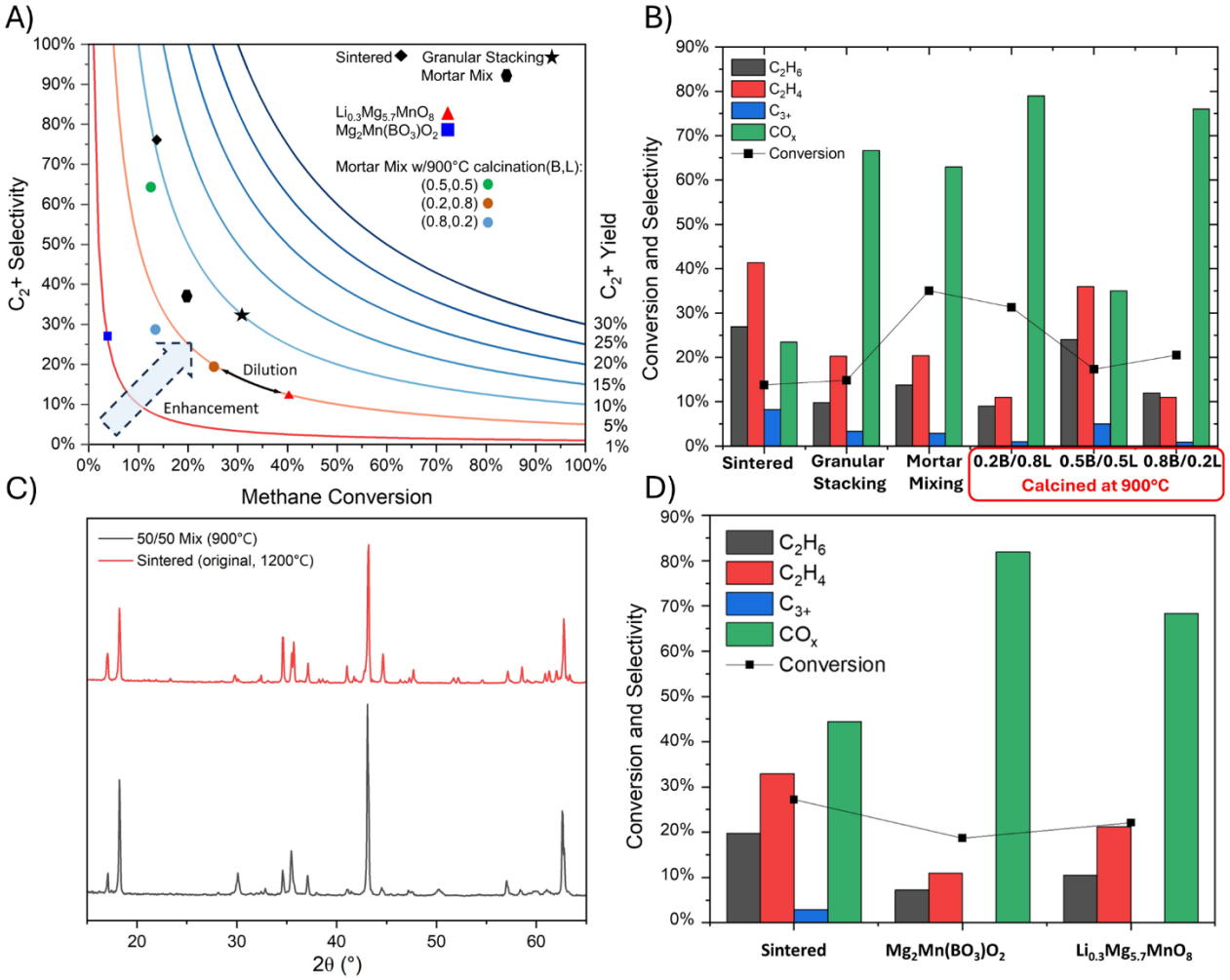

Figure 6. CL-OCM performance at fixed conditions of 840°C, 30s injection time, and 2400 h^{-1} GHSV comparing the **(a)** C_{2+} yields and selectivities vs. conversion, and **(b)** a breakdown of the C_{2+} selectivities for the sintered catalysts: sintered, granular stacking of the catalysts, 45/55 wt.% mortar-ground mixture of the orthoborate oxide phase (B) and the Li-doped phase (L) without calcination, and three different mortar-ground mixture configurations with subsequent 900°C calcination corresponding to 20/80, 50/50, and 80/20 mixtures of B/L phases. **(c)** Comparison of XRD patterns for the original sintered catalyst and the 50/50 mixture. **(d)** Summary of the performance results of the co-feed experiments.

While it is difficult to track the migration of Li^+ in a complex, heterogenous catalyst system considered here, the consequence of Li^+ incorporation into the orthoborate oxide phase can be evaluated. Since it has been established that the $Mg_2Mn(BO_3)O_2$ phase exhibits limited redox capabilities as evidenced by *in situ* XRD analysis (Fig. 4) and CL-OCM experiments (Fig. 6(a&b))

and that oxygen release is a necessary component to CL-OCM activity, steady-state co-feed experiments were conducted on Li-doped and undoped $Mg_2Mn(BO_3)O_2$ using a mixture of 4:1 CH_4:O_2 in N_2 at 840°C (Fig. 6(d)). Compared to the chemical looping (CL) mode, the $Mg_2Mn(BO_3)O_2$ phase demonstrated higher conversion (~19%) with similar selectivity (~20%), ultimately resulting in a higher C_{2+} yield of 3.7% than the CL mode (~1.5%). The introduction of co-fed O_2 enhanced the activity of the less redox-active $Mg_2Mn(BO_3)O_2$ phase. This observation suggests methane activation by $Mg_2Mn(BO_3)O_2$ is limited by the availability of active oxygen species, and combining it with the more redox-active $Li_{0.3}Mg_{5.7}MnO_8$ phase can be a part of achieving the yield enhancement observed. Moreover, the B phase sample doped with Li showed a nearly doubled overall C_{2+} yield of 7.0% with an increase in both selectivity (31.7%) and conversion (22.1%). The exact catalytic role of Li continues to be a topic of debate even in less complex systems. Nonetheless, the physical mixing and steady-state experiments strongly suggest that Li, and its possible migration between phase boundaries, is a vital component to the observed synergy and yield enhancement.

Despite its comparable performance to the classical Mn-Na_2WO_4/SiO_2 family, the redox catalyst system investigated in the current study is rather complex, exhibiting multiple crystalline phases that act cooperatively to enhance the OCM reaction relative to acting individually. At this juncture, this catalyst system remains at a nascent stage of investigation within the OCM community, eluding a definitive description of its catalytic mechanism. However, the *ex situ* and *in situ* characterization results which we have presented in this work, combined with the physical mixing studies, allow for useful conclusions to be drawn, which may guide future studies. We have generated clear evidence that the $Li_xMg_{6-x}MnO_8$ (L) phase is primarily responsible for lattice oxygen donation during the CL-OCM reactions, whereas the $Mg_2Mn(BO_3)O_2$ (B) phase is significantly less redox-active but more selective towards coupling products. The rate of the latter is limited by the availability of active oxygen species, which could be supplied by the adjacent L-phase. Moreover, the migration of Li cation from the L to B phase would promote the catalytic activity and selectivity of the B phase. The interaction of Li with the less redox-active orthoborate oxide phase may alter the active site(s) for methyl radical formation to steer selectivity away from CO_x species, while the labile oxygen release of the $Li_xMg_{6-x}MnO_8$ phase provides the necessary active O species locally to drive the OCM reaction. This explains the significant C_{2+} yield enhancement after intimate mixing and sintering of the two crystalline phases relative to their individual performance. Therefore, an effective catalyst from this OCM catalyst family requires the simultaneous presence and intimate mixing of all the cation components (Mn, Mg, Li, and B), and the optimal portion corresponds to an L-to-B phase weight ratio of approximately 1:1.

4. Conclusions

This present study comprehensively evaluates and characterizes an understudied, yet highly effective dual phase redox catalyst system for CL-OCM. The findings are summarized as follows:

(1) The pre-sintered variant achieved strong CL-OCM performance (26.8% C_{2+} yield) maintained over 30 cycles at 840°C, however, the sintered form displayed superior C_{2+} selectivities when the conditions were the same. Trends in the specific productivity and H_2-TPR measurements

support the idea that these performance discrepancies cannot be solely attributed to reduced surface area.

(2) Bulk characterization of the crystalline structure via XRD with Rietveld refinement revealed notable differences in the proportions between $Li_xMg_{6-x}MnO_8$ and $Mg_{3-x}Mn_x(BO_3)O_2$ between the two catalysts. Specifically, sintering the catalyst more than doubles the mass percentage of the orthoborate oxide phase from ~19% to ~45%. SEM also revealed a profound increase in crystallite size after sintering.

(3) Analysis of the surface region (1-3 nm) via XPS suggests that the average oxidation state of the reducible metal, Mn, is higher for the pre-sintered catalyst, which likely contributes to its overoxidation tendency. Deconvolution of the XPS B 1s spectra showed that boron was predominately in the form of the orthoborate anion (BO_3^{3-}) in the surface region.

(4) CL-OCM experiments conducted on individual pure phases of $Li_{0.3}Mg_{5.7}MnO_8$ and $Mg_2Mn(BO_3)O_2$ as well as on three differently prepared mixtures of these components (granular stacking, mortar-grounded before pelletization with and without additional calcination at 900°C) demonstrate a clear cooperative or synergistic enhancement effect suggesting that both the proportion and site proximity of the two phases influence C_{2+} selectivity.

(5) *In situ* characterization carried out in reducing and oxidizing environments via NAP-XPS, XRD, and Raman spectroscopy provides further evidence for the role of BO_x sites that are formed during the reaction. Specifically, XRD indicated that the orthoborate oxide phase does not change structure during reduction, nor is there a newly formed *in situ* crystalline phase that may explain reactivity trends. Raman showed a clear band corresponding to excited BO_3^{3-}, and NAP-XPS identified a conspicuous high-energy peak arising in the B 1s region during the CH_4 injection segment of the NAP-XPS scans, suggesting that surface boron species are dynamic and may be undergoing hydroxylation under reaction conditions.

(6) While the complexity of such a system poses significant challenges to identify the active sites and specific reaction pathways, our investigations nonetheless generated clear evidence to support that a combination of oxygen release from the more redox-active $Li_xMg_{6-x}MnO_8$ phase, the less-redox active orthoborate oxide species, and Li^+ migration and promotion of the orthoborate oxide are likely behind the observed synergism.

Supporting Information

The supporting information is available free of charge at:

Representative MS plot of CL-OCM cycle, elemental analysis via ICP, additional CL-OCM product breakdown, temperature effects, additional redox property characterization, Rietveld refinement plots and results, additional SEM and TEM micrographs, further breakdown of catalyst bulk and surface composition via HRTEM and XPS, respectively.

Acknowledgments

This work was supported by the US Department of Energy (DE-FE0031869) and the U.S. National Science Foundation (Award No. CBET-1923468). We also acknowledge the support from the Alexander von Humboldt Foundation and the Deutsche Forschungsgemeinschaft (DFG, German Research Foundation) under Germany's Excellence Strategy – EXC 2008/1 (UniSysCat) –

390540038. This work was performed in part at the Analytical Instrumentation Facility (AIF) at North Carolina State University, which is supported by the State of North Carolina and the National Science Foundation (award number ECCS-2025064). This work also made use of instrumentation at AIF acquired with support from the National Science Foundation (DMR-1726294). The AIF is a member of the North Carolina Research Triangle Nanotechnology Network (RTNN), a site in the National Nanotechnology Coordinated Infrastructure (NNCI). The authors thank Astrid Müller-Klauke at TU Berlin for conducting ICP measurements, Chris Winkler at AIF for conducting additional TEM scans, and well as Dennis Chacko at NCSU for providing constructive feedback and minor edits on the manuscript drafts.

References

1. Crabtree, R.H., *Aspects of Methane Chemistry.* Chemical Reviews, 1995. **95**(4): p. 987-1007.
2. Horn, R. and R. Schlögl, *Methane Activation by Heterogeneous Catalysis.* Catalysis Letters, 2014. **145**(1): p. 23-39.
3. McFarland, E., *Unconventional Chemistry for Unconventional Natural Gas.* Science, 2012. **338**(6105): p. 340-342.
4. Keller, G.E., and Bhasin, M.M. , *Synthesis of Ethylene via Oxidative Coupling of Methane.* Journal of Catalysis, 1982. **73**(1): p. 9-19.
5. Galadima, A. and O. Muraza, *Revisiting the oxidative coupling of methane to ethylene in the golden period of shale gas: A review.* Journal of Industrial and Engineering Chemistry, 2016. **37**: p. 1-13.
6. Penteado, A.T., et al., *Techno-economic evaluation of a biogas-based oxidative coupling of methane process for ethylene production.* Frontiers of Chemical Science and Engineering, 2018. **12**(4): p. 598-618.
7. Sokolov, S., et al., *An Approach Using Oxidative Coupling of Methane for Converting Biogas and Acid Natural Gas into High-Calorific Fuels.* Industrial & Engineering Chemistry Research, 2018. **58**(7): p. 2454-2459.
8. Farrell, B.L., V.O. Igenegbai, and S. Linic, *A Viewpoint on Direct Methane Conversion to Ethane and Ethylene Using Oxidative Coupling on Solid Catalysts.* ACS Catalysis, 2016. **6**(7): p. 4340-4346.
9. Stansch, Z., Mleczko, L., and Baerns, M., *Comprehensive Kinetics of Oxidative Coupling of Methane over the La_2O_3/CaO Catalyst* Ind. Eng. Chem. Res., 1997. **36**(7): p. 2568-2579.
10. Driscoll, D.J., and Lunsford, J.H., *Gas-Phase Radical Formation during the Reactions of Methane, Ethane, Ethylene, and Propylene over Selected Oxide Catalysts.* J. Phys. Chem., 1985. **89**(21): p. 4415–4418.
11. Qin, L., et al., *Cyclic redox scheme towards shale gas reforming: a review and perspectives.* Reaction Chemistry & Engineering, 2020. **5**(12): p. 2204-2220.
12. Zhu, X., et al., *Chemical looping beyond combustion – a perspective.* Energy & Environmental Science, 2020. **13**(3): p. 772-804.
13. Chung, E.Y., et al., *Catalytic Oxygen Carriers and Process Systems for Oxidative Coupling of Methane Using the Chemical Looping Technology.* Industrial & Engineering Chemistry Research, 2016. **55**(50): p. 12750-12764.
14. Jiang, T., et al., *La_2O_3 catalysts with diverse spatial dimensionality for oxidative coupling of methane to produce ethylene and ethane.* RSC Advances, 2016. **6**(41): p. 34872-34876.
15. Siakavelas, G.I., et al., *Cerium oxide catalysts for oxidative coupling of methane reaction: Effect of lithium, samarium and lanthanum dopants.* Journal of Environmental Chemical Engineering, 2022. **10**(2).
16. Zhao, K., et al., *Lithium carbonate-promoted mixed rare earth oxides as a generalized strategy for oxidative coupling of methane with exceptional yields.* Nat Commun, 2023. **14**(1): p. 7749.

17. Jiang, Z.-C., Hua, G., and Li, S.-B., *Methane activation over Mn_2O_3-Na_2WO_4/SiO_2 catalyst and oxygen spillover.* Studies in surface science and catalysis, 1997. **112**: p. 481-490
18. Xueping, F., Shuben, L., Jingzhu, L., Jingfang, G., and Dexin, Y., *Preparation and Characterization of Catalyst for Oxidative Coupling of Methane.* J. Mol. Catal., 1992. **6**(2).
19. Arndt, S., et al., *Mn–Na_2WO_4/SiO_2 as catalyst for the oxidative coupling of methane. What is really known?* Applied Catalysis A: General, 2012. **425-426**: p. 53-61.
20. Sourav, S., et al., *Molecular structure and catalytic promotional effect of Mn on supported Na_2WO_4/SiO_2 catalysts for oxidative coupling of methane (OCM) reaction.* Catalysis Today, 2022.
21. Wachs, I.E., *Progress in catalysis by mixed oxides: From confusion to catalysis science.* Catalysis Today, 2022.
22. Wu, J., and Li, S., *The Role of Distorted WO4 in the Oxidative Coupling of Methane on Supported Tungsten Oxide Catalysts.* J. Phys. Chem., 1995. **99**: p. 4566-4568.
23. Wang, P., et al., *TiO_2-doped Mn_2O_3-Na_2WO_4/SiO_2 catalyst for oxidative coupling of methane: Solution combustion synthesis and $MnTiO_3$-dependent low-temperature activity improvement.* Applied Catalysis A: General, 2017. **544**: p. 77-83.
24. Arndt, S., et al., *A Critical Assessment of Li/MgO-Based Catalysts for the Oxidative Coupling of Methane.* Catalysis Reviews, 2011. **53**(4): p. 424-514.
25. Yusuf, S., et al. , *Effects of Sodium and Tungsten Promoters on Mg_6MnO_8 Based Core-Shell Redox Catalysts for Chemical Looping – Oxidative Dehydrogenation of Ethane.* ACS Catal, 2019. **9**(4): p. 3174-3186.
26. Baser, D.S., et al., *Codoping Mg-Mn Based Oxygen Carrier with Lithium and Tungsten for Enhanced C_2 Yield in a Chemical Looping Oxidative Coupling of Methane System.* ACS Sustainable Chemistry & Engineering, 2021. **9**(7): p. 2651-2660.
27. Cheng, Z., et al., *C_2 Selectivity Enhancement in Chemical Looping Oxidative Coupling of Methane over a Mg–Mn Composite Oxygen Carrier by Li-Doping-Induced Oxygen Vacancies.* ACS Energy Letters, 2018. **3**(7): p. 1730-1736.
28. Sofranko, J.A., Gastinger, R.G., and Jones, A. , *Boron-Promoted Reducible Metal Oxides And Methods Of Their Use*, T.U.S.P.a.T. Office, Editor. 1988, Atlantic Richfield Company, US4777313: U.S.A.
29. Sofranko, J.A., *Stabilized Oxyborates and their use for Oxidative Conversion of Hydrocarbons*. 2021, EcoCatalytic Inc, US10919027: U.S.A.
30. Buyevskaya, O.V., et al., *Selective Oxidative Conversion of Propane to Olefins and Oxygenates on Boria-Containing Catalysts*, in *Natural Gas Conversion V, Proceedings ofthe 5th International Natural Gas Conversion Symposium*. 1998. p. 671-676.
31. Grant, J.T., et al., *Boron and Boron-Containing Catalysts for the Oxidative Dehydrogenation of Propane.* ChemCatChem, 2017. **9**(19): p. 3623-3626.
32. Lu, W.-D., et al., *Supported Boron Oxide Catalysts for Selective and Low-Temperature Oxidative Dehydrogenation of Propane.* ACS Catalysis, 2019. **9**(9): p. 8263-8270.
33. Love, A.M., et al., *Synthesis and Characterization of Silica-Supported Boron Oxide Catalysts for the Oxidative Dehydrogenation of Propane.* The Journal of Physical Chemistry C, 2019. **123**(44): p. 27000-27011.
34. Zhang, X., et al., *Radical Chemistry and Reaction Mechanisms of Propane Oxidative Dehydrogenation over Hexagonal Boron Nitride Catalysts.* Angew Chem Int Ed Engl, 2020. **59**(21): p. 8042-8046.
35. Qian, H., et al., *Efficient metal borate catalysts for oxidative dehydrogenation of propane.* Catalysis Science & Technology, 2022. **12**(6): p. 1996-2005.
36. Zhang, Z., Hermans, I., Alexandrova, A.N., *Off-stoichiometric Restructuring and Sliding Dynamics of Hexagonal Boron Nitride Edges in Conditions of Oxidative Dehydrogenation of Propane.* 2023.
37. Grant, J.T., Carrero, C.A., Goeltl, F., Venegas, J., Mueller, P., Burt, S.P., Spect, S.E., McDermott, W.P., Chieregato, A., and Hermans, I., *Selective oxidative dehydrogenation of propane to propene using boron nitride catalysts.* Science, 2016. **354**(6319): p. 1570-1573.

38. Shi, L., Yan, B., Shao, D., Jiang, F., Wang, D., and Lu, A-H., *Selective oxidative dehydrogenation of ethane to ethylene over a hydroxylated boron nitride catalyst.* Chinese Journal of Catalysis, 2017. **38**(2): p. 389-395.
39. Shi, L., et al., *Progress in selective oxidative dehydrogenation of light alkanes to olefins promoted by boron nitride catalysts.* Chem Commun (Camb), 2018. **54**(78): p. 10936-10946.
40. Loiland, J.A., et al., *Boron-Containing Catalysts for the Oxidative Dehydrogenation of Ethane/Propane Mixtures.* Industrial & Engineering Chemistry Research, 2019. **58**(6): p. 2170-2180.
41. Wang, Y., et al., *Methane activation over a boron nitride catalyst driven by in situ formed molecular water.* Catalysis Science & Technology, 2018. **8**(8): p. 2051-2055.
42. Han, P., et al., *Mechanistic Insights into Radical-Induced Selective Oxidation of Methane over Nonmetallic Boron Nitride Catalysts.* J Am Chem Soc, 2023. **145**(19): p. 10564-10575.
43. Toby, B.H. and R.B. Von Dreele, *GSAS-II: the genesis of a modern open-source all purpose crystallography software package.* Journal of Applied Crystallography, 2013. **46**(2): p. 544-549.
44. Ilton, E.S., et al., *XPS determination of Mn oxidation states in Mn (hydr)oxides.* Applied Surface Science, 2016. **366**: p. 475-485.
45. Biesinger, M.C., et al., *Resolving surface chemical states in XPS analysis of first row transition metals, oxides and hydroxides: Cr, Mn, Fe, Co and Ni.* Applied Surface Science, 2011. **257**(7): p. 2717-2730.
46. Ge, R., et al., *Cobalt-Borate Nanoarray: An Efficient and Durable Electrocatalyst for Water Oxidation under Benign Conditions.* ACS Appl Mater Interfaces, 2017. **9**(18): p. 15383-15387.
47. Dastafkan, K., et al., *Enhanced surface wettability and innate activity of an iron borate catalyst for efficient oxygen evolution and gas bubble detachment.* Journal of Materials Chemistry A, 2019. **7**(25): p. 15252-15261.
48. He, C., X. Wu, and Z. He, *Amorphous Nickel-Based Thin Film As a Janus Electrocatalyst for Water Splitting.* The Journal of Physical Chemistry C, 2014. **118**(9): p. 4578-4584.
49. Zhou, F., et al., *Investigation on microstructure and its transformation mechanisms of B_2O_3-SiO_2-Al_2O_3-CaO brazing flux system.* High Temperature Materials and Processes, 2020. **39**(1): p. 88-95.
50. Wang, Y., and Trenary, M., *Surface Chemistry of Boron Oxidation. 2. The Reactions of B_2O_2 and B_2O_3 with Boron Films Grown on Ta(110).* Chem. Mater., 1993. **5**(2): p. 199-205.
51. Runka, T. and M. Berkowski, *Perovskite $La_{1-x}Sr_xGa_{1-y}Mn_yO_3$ solid solution crystals: Raman spectroscopy characterization.* Journal of Materials Science, 2012. **47**(14): p. 5393-5401.
52. Julien, C., *Raman spectra of birnessite manganese dioxides.* Solid State Ionics, 2003. **159**(3-4): p. 345-356.
53. Post, J.E., D.A. McKeown, and P.J. Heaney, *Raman spectroscopy study of manganese oxides: Layer structures.* American Mineralogist, 2021. **106**(3): p. 351-366.
54. Meera, B.N., Sood, A.K., Chandrabhas, N., and Ramakrishna, J., *Raman study of lead borate glasses.* Journal of Non-Crystalline Solids, 1990. **126**(3): p. 224-230.
55. Dwivedi, B.P., Rahman, M.H., Kumar, Y., and Khana, B.N., *Raman Scattering Study of Lithium Borate Glasses.* J. Phys. Chem. Solids, 1993. **54**: p. 621-628.
56. Frost, R.L., et al., *Infrared and Raman spectroscopic characterization of the borate mineral hydroboracite $CaMg[B_3O_4(OH)_3]_2{\cdot}3H_2O$ – Implications for the molecular structure.* Journal of Molecular Structure, 2014. **1059**: p. 20-26.
57. Yadav, A.K., and Singh, P., *A review of the structures of oxide glasses by Raman spectroscopy.* RSC Advances, 2015. **5**(83): p. 67583-67609.

For Table of Contents Only